Low Mach number flow induced noise prediction of wall mounted airfoil using a hybrid RANS-BEM technique

P. Croaker, D. Moreau, M. Karimi, N. Kessissoglou

School of Mechanical & Manufacturing Engineering, UNSW Australia, Sydney, Australia

ABSTRACT

A hybrid RANS-BEM technique for the prediction of low Mach number flow induced noise produced by a body immersed in the flow is presented. A steady-state Reynolds Averaged Navier-Stokes (RANS) simulation is used to obtain turbulence statistics and mean flow data of the flow. Statistical noise sources are then determined from the mean flow and turbulence statistics by employing a model for the turbulence cross spectrum. These noise sources are then combined with a boundary element method (BEM) model of the body to predict the aeroacoustic scattering and the far-field noise. The hybrid RANS-BEM technique is applied to predict the flow-induced noise produced by flow past a wall mounted NACA0012 airfoil, with Reynolds number based on chord of Re_c=1.1 $\times$ 10^6 and a Mach number of M=0.12 at zero angle of attack. The results are in good agreement with experimental results.

1. INTRODUCTION

Flow past a marine vessel is characterised by low Mach numbers and very high Reynolds numbers. Accurately resolving wall-bounded flow at these Reynolds numbers requires a high fidelity mesh. Traditional flow-induced noise techniques require time resolved hydrodynamic data to calculate the flow noise sources (Wang and Moin, 2000; Wang *et al.*, 2009; Khalighi *et al.*, 2010). Computing time resolved hydrodynamics on a high fidelity mesh is computationally demanding in terms of both data storage and simulation time.

An attractive alternative is to develop models to predict fluctuating flow noise sources based on the turbulence statistics available from a steady-state RANS simulation. Doolan *et al.* (2010) proposed a RANS based statistical noise model (RSNM) that uses an assumed turbulent velocity cross spectrum defined in terms of RANS mean flow data to characterise the flow noise sources in the boundary layer. Turbulent velocity cross spectra can be obtained experimentally (Fleury *et al.*, 2008), predicted numerically from a transient fluid dynamics simulation (He *et al.*, 2008) or modelled using analytical or empirical models (Doolan *et al.*, 2010; Zhao and He, 2009).

Many of the control surfaces and appendages of a marine vessel have relatively thick profiles. Accurately resolving the scattering from such appendages requires a technique such as the boundary element method (Khalighi *et al.*, 2010). Hybrid computational fluid dynamics (CFD) - BEM techniques applied to aeroacoustic scattering typically extract acoustic sources from transient CFD simulations (Khalighi *et al.*, 2010; Croaker *et al.*, 2015). In contrast, Ostertag *et al.* (2000) extract flow noise sources from steady state RANS data rather than transient CFD data. They then use a BEM technique to predict the aeroacoustic scattering from the RANS data. Monopole sources were placed at each field point location and the acoustic pressure at each source point was recorded. The double spatial derivative of a volume distribution of the acoustic pressure at the source points were calculated and the reciprocal theorem was used to determine the tailored Green's function of the body. The disadvantage of this approach is that significant errors can be introduced by spatial discretisation and differentiation on a numerical grid (Crighton, 1988).

This paper presents a hybrid RANS-BEM technique to predict flow-induced noise produced by turbulent flow past a body. The incident acoustic field produced by statistical flow noise sources are calculated using a recently derived formulation for the near-field pressure (Croaker *et al.*, 2015). This incident pressure is then applied to a BEM-based prediction of the scattered sound by the body. To demonstrate the hybrid RANS-BEM technique, the far-field sound produced by turbulent flow over a finite wall-mounted airfoil with Reynolds number based on the chord of Re_c=1.1 $\times$ 10^6 and Mach number of M=0.12 is predicted.

2. NUMERICAL PROCEDURE

2.1 Incident Pressure from a Single Turbulent Source

To determine the far-field pressure produced by the scattering of flow induced noise by a rigid body, the incident pressure on the body is calculated using (Croaker *et al.*, 2015):

$$p_{\text{inc}}(\mathbf{x},\omega) = \lim_{\varepsilon\to 0}\int_{(\Omega-V_\varepsilon)} \rho_f U_i(\mathbf{y})\, U_j(\mathbf{y})\, \frac{\partial^2 G_h(\mathbf{x},\mathbf{y})}{\partial y_i \partial y_j} d\mathbf{y} \tag{1}$$

where $p_{\text{inc}}(\mathbf{x},\omega)$ is the Fourier transform of the incident pressure at field point $\mathbf{x}$ and angular frequency ω. ρ_f is the density of the fluid. $U_i(\mathbf{y})$ is the fluid velocity in the i^{th} direction at the source point $\mathbf{y}$ and consists of a mean component $\bar{U}_i(\mathbf{y})$ and a fluctuating component $u_i^{'}(\mathbf{y})$ as follows

$$U_i(\mathbf{y}) = \bar{U}_i(\mathbf{y}) + u_i^{'}(\mathbf{y}) \tag{2}$$

Ω is the computational domain occupied by the flow noise sources and V_ε represents an exclusion neighbourhood around the field point $\mathbf{x}$. This exclusion neighbourhood allows the singularities occurring when $\mathbf{x} = \mathbf{y}$ to be regularised. The harmonic free-field Green's function is given by

$$G_h = \frac{e^{\mathrm{i}k_a r}}{4\pi r} \tag{3}$$

and in two dimensions by

$$G_h = \frac{\mathrm{i}}{4} H_0^{(1)}\left(k_a r\right) \tag{4}$$

where k_a is the acoustic wave number, $r = \|\mathbf{x} - \mathbf{y}\|$ is the distance between the source and field points and $\mathrm{i} = \sqrt{-1}$. $H_0^{(1)}$ is a Hankel function of the first kind of order zero. In equation (1), the contribution from viscous stresses has been neglected as only high Reynolds number flows are considered.

In the proceeding derivation, the limit in equation (1) is omitted. The singularity regularisation outlined in Croaker *et al.* (2015) is followed. Decomposing equations (1) into contributions from individual CFD cells produces

$$\begin{aligned} p_{\mathrm{inc}}\left(\mathbf{x},\omega\right) &= \sum_{c=1}^{C} p_{c,\mathrm{inc}}\left(\mathbf{x},\omega\right) \\ &= \sum_{c=1}^{C} \int_{\Omega_c} \rho_f U_{i,c}\left(\mathbf{y}\right) U_{j,c}\left(\mathbf{y}\right) \frac{\partial^2 G_h\left(\mathbf{x},\mathbf{y}\right)}{\partial y_i \partial y_j} d\Omega_c \end{aligned} \tag{5}$$

where $p_{c,\mathrm{inc}}\left(\mathbf{x},\omega\right)$ is the Fourier transform of the incident pressure due to the c^{th} CFD cell. $U_{i,c}\left(\mathbf{y}\right)$ is the fluid velocity in the i^{th} direction at position $\mathbf{y}$ of CFD cell c. Ω_c is the computational domain occupied by the c^{th} CFD cell and C is the total number of CFD cells. Assuming the fluid is incompressible and that the velocity is constant over the domain Ω_c, $p_{c,\mathrm{inc}}\left(\mathbf{x},\omega\right)$ can be represented by

$$p_{c,\mathrm{inc}}\left(\mathbf{x},\omega\right) = \rho_f\, U_{i,c}\left(\mathbf{y}\right) U_{j,c}\left(\mathbf{y}\right) \int_{\Omega_c} \frac{\partial^2 G_h\left(\mathbf{x},\mathbf{y}\right)}{\partial y_i \partial y_j} d\Omega_c \tag{6}$$

where ρ_f is the density of the fluid at rest. The following approximations for the Lighthill tensor can be used (Ffowcs Williams and Hall, 1970)

$$\rho_f U_{i,c}\left(\mathbf{y}\right) U_{j,c}\left(\mathbf{y}\right) \approx \rho_f \bar{U}_{i,c} u_{j,c}^{'} + \rho_f \bar{U}_{j,c} u_{i,c}^{'} \tag{7}$$

Anisotropy is introduced into the model by considering

$$u_{i,c}^{'} = u_{s,c} f_{i,c} \tag{8}$$

where $u_{s,c}$ and $f_{i,c}$ are the characteristic velocity of the turbulence and the anistropy factor for the i^{th} velocity component of the c^{th} CFD cell. Setting $f_{i,c} = 1$ reproduces isotropic turbulence. Equation (6) can then be expressed as

$$p_{c,\mathrm{inc}}\left(\mathbf{x},\omega\right) = \left(\rho_f \bar{U}_{i,c} u_{s,c} f_{j,c} + \rho_f \bar{U}_{j,c} u_{s,c} f_{i,c}\right) \int_{\Omega_c} \frac{\partial^2 G_h\left(\mathbf{x},\mathbf{y}\right)}{\partial y_i \partial y_j} d\Omega_c \tag{9}$$

A velocity normalised incident pressure $\hat{p}_{c,\mathrm{inc}}$ is obtained by dividing the incident pressure $p_{c,\mathrm{inc}}$ by $u_{s,c}$ to give

$$\hat{p}_{c,\mathrm{inc}}\left(\mathbf{x},\omega\right) = \left(\rho_f \bar{U}_{i,c} f_{j,c} + \rho_f \bar{U}_{j,c} f_{i,c}\right) \int_{\Omega_c} \frac{\partial^2 G_h\left(\mathbf{x},\mathbf{y}\right)}{\partial y_i \partial y_j} d\Omega_c \tag{10}$$

Equation (10) is solved using the near-field formulation for pressure derived previously by the authors and described in detail in Croaker *et al.* (2015).

2.2 Scattered Pressure Field using the BEM

The non-homogeneous Helmholtz equation is given by (Marburg and Nolte, 2008)

$$\triangle p_c\left(\mathbf{x},\omega\right) + k_a^2 p_c\left(\mathbf{x},\omega\right) = -q \tag{11}$$

where $p_c\left(\mathbf{x},\omega\right)$ is the acoustic pressure at field point $\mathbf{x}$ and q is an acoustic source. A solution of the non-homogeneous Helmholtz equation can be obtained by calculating the incident pressure on the body radiated by the source and applying it as a load to the boundary integral equation as follows (Marburg and Nolte, 2008)

$$\begin{aligned} c\left(\mathbf{y}\right) p_c\left(\mathbf{y},\omega\right) = &-\int_{\Gamma} \frac{\partial G_h\left(\mathbf{x},\mathbf{y}\right)}{\partial n\left(\mathbf{x}\right)} p_c\left(\mathbf{x},\omega\right) d\Gamma\left(\mathbf{x}\right) \\ &+ \mathrm{i}\rho_f c_f k_a \int_{\Gamma} G_h\left(\mathbf{x},\mathbf{y}\right) v_c\left(\mathbf{x},\omega\right) d\Gamma\left(\mathbf{x}\right) + p_{c,\mathrm{inc}}\left(\mathbf{y},\omega\right) \end{aligned} \tag{12}$$

where c_f is the speed of sound in the fluid. Γ is the surface of the body and $\mathbf{n}$ is a unit vector in the direction normal to the body. $c(\mathbf{y})$ is a free-term coefficient equal to 1 in the domain interior and 0.5 on a smooth boundary. v_c is the fluid particle velocity. Using the hybrid RANS-BEM approach, both sides of equation (12) are divided by $u_{s,c}$ to yield

$$c(\mathbf{y})\,\hat{p}_c(\mathbf{y},\omega) = -\int_\Gamma \frac{\partial G_h(\mathbf{x},\mathbf{y})}{\partial n(\mathbf{x})}\hat{p}_c(\mathbf{x},\omega)\,d\Gamma(\mathbf{x}) + \mathrm{i}\rho_f c_f k_a \int_\Gamma G_h(\mathbf{x},\mathbf{y})\,\hat{v}_c(\mathbf{x},\omega)\,d\Gamma(\mathbf{x}) + \hat{p}_{c,\mathrm{inc}}(\mathbf{y},\omega) \tag{13}$$

where $\hat{p}_c$ is velocity normalised scattered pressure on the body due to the flow noise source in the c^{th} CFD cell. $\hat{v}_c(\mathbf{x},\omega)$ is the velocity normalised particle velocity on the body arising from the flow noise source in cell c. The normal derivative of the normalised pressure is constrained to zero on the body to represent a rigid body.

The velocity normalised scattered pressure in the far-field $\hat{p}_c(\mathbf{x_f},\omega)$ due to the flow noise source in the c^{th} CFD cell can be determined by solving

$$\hat{p}_c(\mathbf{x_f},\omega) = -\int_\Gamma \frac{\partial G_h(\mathbf{x},\mathbf{y})}{\partial n(\mathbf{x})}\hat{p}_c(\mathbf{x},\omega)\,d\Gamma(\mathbf{x}) \tag{14}$$

where $\mathbf{x_f}$ is the far-field point. The far-field scattered pressure $p_c(\mathbf{x_f},\omega)$ can then be obtained by

$$p_c(\mathbf{x_f},\omega) = u_{s,c}\hat{p}_c(\mathbf{x_f},\omega) \tag{15}$$

The scattered field is obtained by solving equations (13)-(15) with the BEM for each CFD cell.

2.3 Far-Field Power Spectral Density

The power spectral density (PSD) $S(\mathbf{x_f},\omega)$ at the far-field point $\mathbf{x_f}$ is calculated by the double summation as follows

$$S(\mathbf{x_f},\omega) = \sum_{b=1}^{C}\sum_{c=1}^{C} p_b(\mathbf{x_f},\omega)\,p_c^*(\mathbf{x_f},\omega) \tag{16}$$

where C is the total number of CFD cells and * indicates the complex conjugate. Substituting equations (15) into equation (16) yields

$$S(\mathbf{x_f},\omega) = \sum_{b=1}^{C}\sum_{c=1}^{C} \Phi(\mathbf{y}_b,\mathbf{y}_c,\omega)\left[\hat{p}_b(\mathbf{x_f},\omega)\,\hat{p}_c^*(\mathbf{x_f},\omega)\right] \tag{17}$$

where $\Phi(\mathbf{y}_b,\mathbf{y}_c,\omega) = \left[u_{s,b}\,u_{s,c}^*\right]$ is the turbulent velocity cross spectrum and is the only unknown quantity in the model.

2.4 Turbulent Velocity Cross Spectrum

Using the theory for homogeneous, isotropic turbulence, the longitudinal and lateral correlation coefficients are given the following Gaussian form (Ewert, 2008)

$$f(r_{bc}) = \exp\left(-\frac{\pi}{4}\frac{r_{bc}^2}{l_s^2}\right) \tag{18}$$

$$g(r_{bc}) = \left(1-\frac{\pi}{4}\frac{r_{bc}^2}{l_s^2}\right)\exp\left(-\frac{\pi}{4}\frac{r_{bc}^2}{l_s^2}\right) \tag{19}$$

where r_{bc} is the distance separating CFD cells b and c. The resulting cross spectrum is given by

$$\Phi(\mathbf{y}_b,\mathbf{y}_c,\omega) = \frac{Au_s^2}{\omega_s}\left(\frac{f(r_{bc})-g(r_{bc})}{r_{bc}^2}r_{bc,i}r_{bc,j} + \delta_{ij}g(r_{bc})\right)\exp\left(-\frac{\omega^2}{\pi\omega_s^2}\right) \tag{20}$$

where $r_{bc,i}$ is the i^{th} derivative of the distance r_{bc} and A is a correlation strength parameter. The other model parameters are linked to the RANS simulation at each cell using the following expressions (Doolan *et al.*, 2010)

$$u_s = \sqrt{\frac{2k}{3}}, \qquad l_s = \frac{c_l k^{3/2}}{\varepsilon}, \qquad \omega_s = c_\omega \frac{u_s}{l_s} \tag{21}$$

where k is the turbulent kinetic energy, ε is the turbulent dissipation rate and c_l and c_ω are semi-empirical parameters. For the case considered here, a correlation strength parameter of $A = 1$ was found by trial and error to produce good agreement between numerical and experimental results.

2.5 CFD Model

A wall mounted NACA0012 airfoil at zero degree angle of attack was modelled. The airfoil has an aspect ratio of 1 with the chord and span both equal to 0.4 m and is located in a square tunnel with side length 1.85 m. A three-dimensional CFD model is used to predict the mean values and turbulence statistics of the flow past the wall mounted airfoil. The computational domain extends 3.4 m upstream of the airfoil's leading edge and 7.3 m downstream of the trailing edge. The boundary layer mesh on the airfoil and tunnel floor is well resolved, with $y^+ \sim 1$ for the cells immediately adjacent to the airfoil. No wall functions were used for these cells. An incompressible flow field past the wall mounted airfoil is simulated with FLUENT at a Reynolds number based on chord of Re_c=1.1×10^6. Moreau *et al.* (2016) conducted experiments on the same wall mounted airfoil in the Stability Wind Tunnel at Virginia Tech.

The inlet velocity was set to 40 m/s on the upstream boundary, with a turbulence intensity of 0.03%, which matches the turbulence intensity at the inflow plane of the experimental facility used by Moreau *et al.* (2016). A zero average pressure boundary condition was imposed at the outlet. A no-slip condition was applied on the surface of the body and the tunnel floor. A free-slip boundary condition is used for the remaining boundaries. The $k-\omega$ SST turbulence model was applied. The mesh contains approximately 6.5×10^6 hexahedral cells. Figure 1 (a) shows an image of the airfoil surface and the surrounding tunnel floor. Figure 1 (b) and (c) show mesh details of the airfoil leading edge near the wall junction and airfoil tip, respectively. Figure 1 (d) shows the mesh detail of the trailing edge of the airfoil tip.

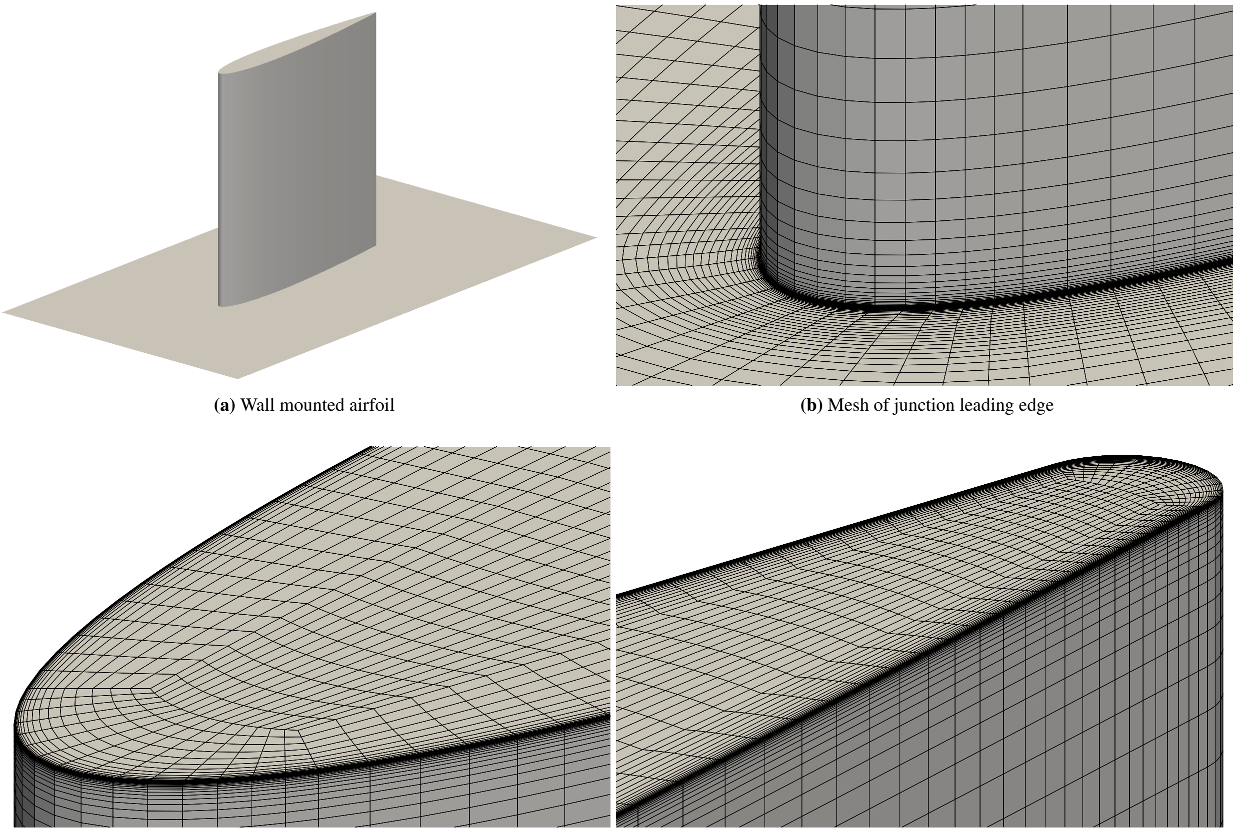

(a) Wall mounted airfoil **(b)** Mesh of junction leading edge

(c) Mesh of tip leading edge **(d)** Mesh of tip trailing edge

Figure 1: CFD mesh for the wall mounted airfoil

2.6 BEM Model

A three-dimensional BEM model was constructed using linear, discontinuous boundary elements. A greater concentration of boundary elements were placed around the leading edge and trailing edges to ensure that interaction of the incident field with the geometry is accurately captured. Figure 2 shows the boundary element mesh of the wall mounted foil. A half space Green's function was used to account for reflection of sound waves by the tunnel floor.

The collocation points of these BEM elements also represent the field points used to calculate the incident normalised pressure using equation (10). Equations (10) and (13) are solved once for each CFD cell. The far-field power spectral density is then calculated by solving equation (17). This suggests that a separate BEM solution is required for every CFD cell which would render the proposed method inefficient. To overcome this, an LU decomposition of the BEM matrices must be performed only once for all CFD cells. The scattered far-field pressures produced by each incident normalised pressure field are then obtained by solving the decomposed matrix by forward and back substitution operations.

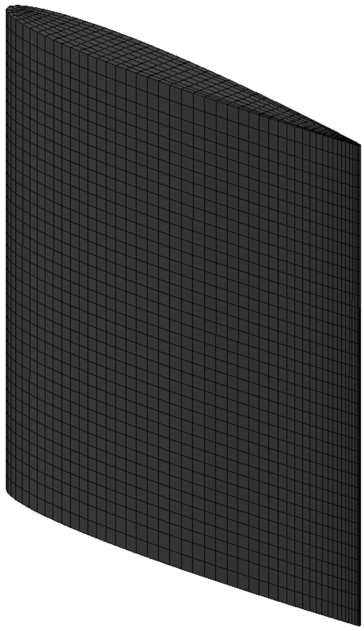

Figure 2: Boundary element mesh of wall mounted airfoil

3. RESULTS

3.1 Turbulent Flow Field

Figure 3 shows the flow structures present around the wall mounted foil. Contour surfaces of constant Q-criterion are used to identify the main structures in the flow. The Q-criterion surfaces are coloured by vorticity magnitude. The flow structures at the junction and the tip are depicted in Figure 3 (a) and Figure 3 (b), respectively. Figure 3 (a) shows that a horseshoe vortex forms upstream of the leading edge at the junction and travels downstream either side of the foil. Near the trailing edge at the junction there is a small separated region which causes the horseshoe vortex to thicken downstream of the trailing edge. Figure 3 (b) shows the formation of vortices along both sides of the airfoil tip and their interaction at the tip trailing edge.

Figure 4 shows the evolution of the characteristic velocity, length and frequency scales of the turbulence, given by equations 21, at several spanwise locations close to the junction. The spanwise locations are represented by z/s, where z is the distance from the wall and s is the span of the airfoil. The velocity and length scales associated with the horseshoe vortex are clearly observed close to the wall near the leading edge. In general, the velocity and length scales are observed to increase through the boundary layer of the wall, while the frequency scales decrease as the distance from the wall increases. Figure 5 shows the evolution of the characteristic velocity, length and frequency scales in the vicinity of the airfoil tip. The vortices generated by the edges of the tip interact with each other at the trailing edge to produce complex flow structures. The turbulence at the edges of the airfoil tip is characterised by high intensity fluctuations which have a small length scale and high frequency scale. Figure 5 shows that the length scale of these fluctuations increases as they travel downstream and the frequency scale decreases. Also, these airfoil tip flow structures are observed to interact with the turbulent boundary layer over the airfoil and influence the thickness of the boundary layer at the trailing edge of the airfoil. The characteristic velocity, length and frequency scales do not vary noticeably in the mid-span of the airfoil as they are outside the influence of the flow structures present at the junction and tip.

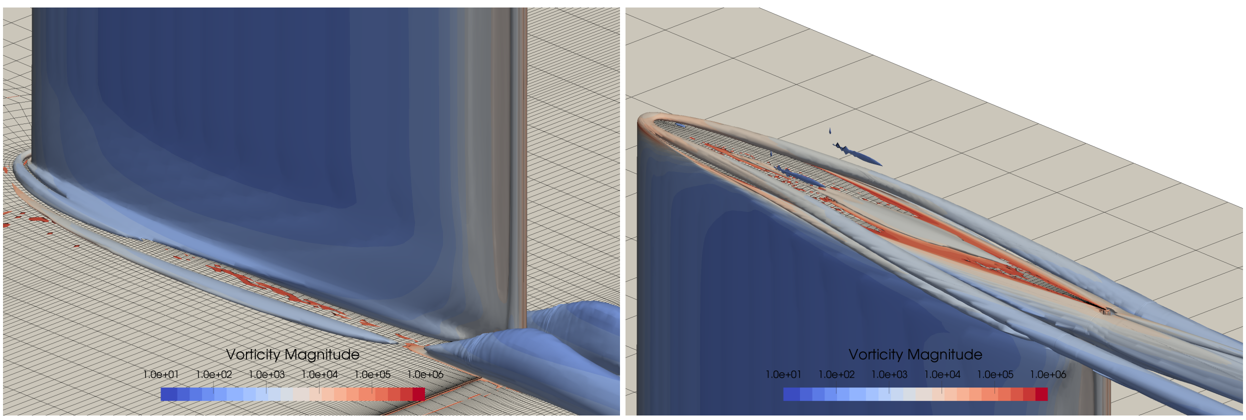

(a) Junction **(b)** Tip

Figure 3: Flow structures around the wall mounted foil. Q-criterion iso surfaces coloured by vorticity magnitude

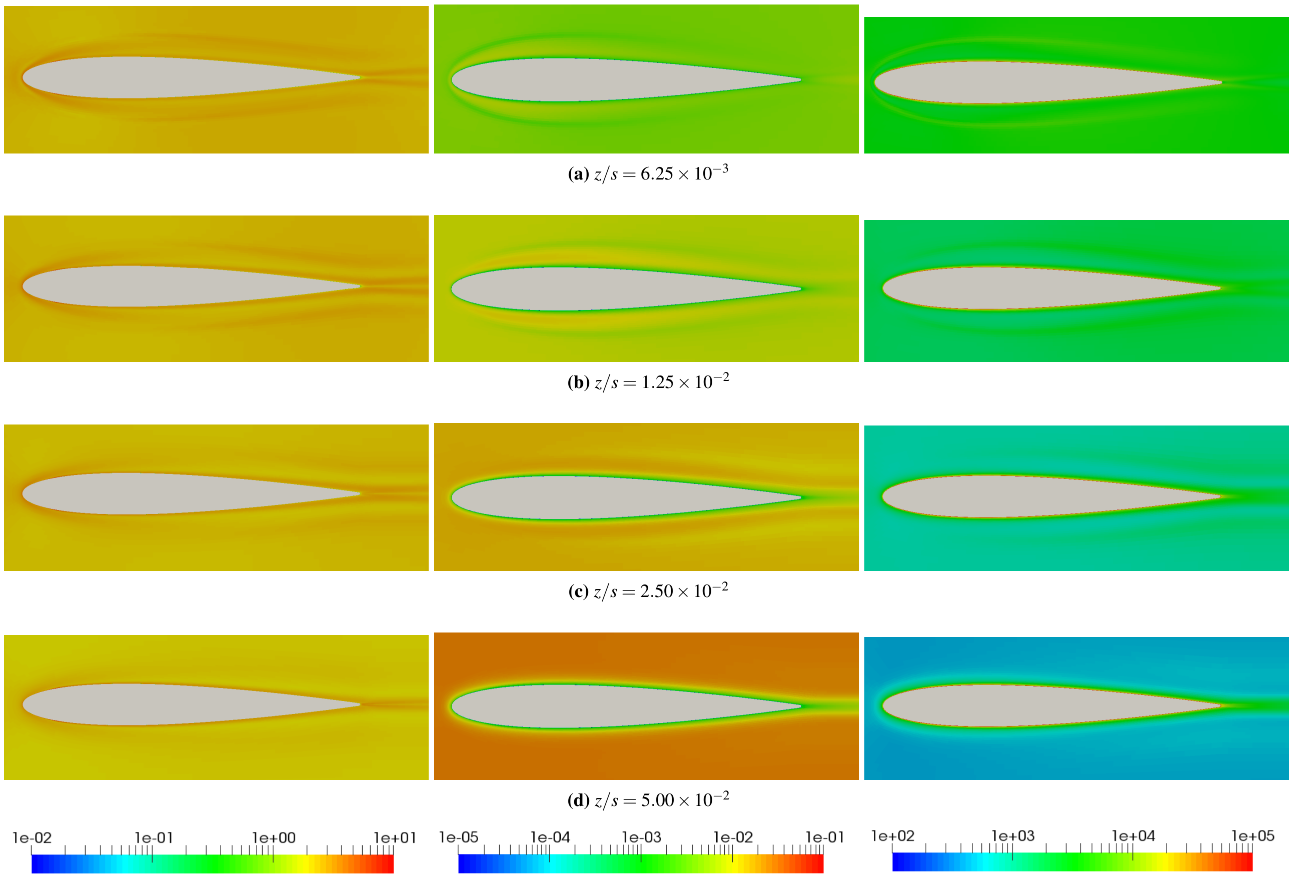

(a) $z/s = 6.25 \times 10^{-3}$

(b) $z/s = 1.25 \times 10^{-2}$

(c) $z/s = 2.50 \times 10^{-2}$

(d) $z/s = 5.00 \times 10^{-2}$

Figure 4: Characteristic velocity (left), length (center) and frequency (right) scales at spanwise planes close to the junction

3.2 Acoustic Results

The turbulence statistics predicted with the RANS simulation are used to compute the turbulent velocity cross spectra. The turbulent velocity cross spectra are then applied to the normalised far-field pressures of equation (17) to predict the power spectral density of the far-field scattered pressure. The far-field sound pressure is predicted at a single location 0.93 m above the floor and 1.92 m away from the airfoil. This location corresponds to the centre of the microphone array used in the experiments of Moreau *et al.* (2016). The array consisted of 117 Panasonic model WM-64PNT Electret microphones arranged in a nine-armed spiral. These microphones have a flat frequency response from 20 to 16,000 Hz. Each of the microphone signals were acquired at a sampling frequency of 51,200 Hz for a sample time of 32 s. The microphone signals were transformed to the frequency domain using a fast Fourier transformation with 200 blocks of 8192 samples per block, resulting in a spectral estimate 95 percent confidence interval of -0.583/+0.625 dB. To obtain the sound maps, frequency domain beamforming was conducted in one-twelfth-octave-bands with diagonal removal. One-twelfth-octave-band acoustic spectra have then been estimated by integrating the sound map over a region of interest.

Figure 6 compares the one-twelfth-octave band sound pressure levels predicted with the present RANS-BEM technique with the experimental results of Moreau *et al.* (2016). Figure 6 shows that the main characteristics of the far-field sound spectra are well captured with the RANS-BEM technique. The sound pressure level is at a maximum at the lowest frequencies and then reduces slightly with increasing frequency. At approximately 1.3 kHz there is a broadband hump in the sound pressure level followed by a reduction in level as the frequency increases. There is good overall agreement between numerical prediction and experimental measurements across the entire frequency range considered here.

4. SUMMARY

The flow-induced noise generated by turbulent flow past a wall mounted airfoil at a Reynolds number based on the chord of $Re_c = 1.1 \times 10^6$ and a Mach number of $M = 0.11$ has been predicted using a hybrid RANS-BEM technique. The flow field data from a steady state RANS simulation is processed by a statistical noise model to estimate the turbulent velocity cross spectrum. The turbulent velocity cross spectrum are then combined with a boundary element model to predict the scattering of the flow induced sound by the body. The far-field sound predicted with the RANS-BEM technique agrees well with experimental results. The RANS-BEM technique automatically resolves all scattering paths from the flow noise sources to the far field. The broadband hump associated with trailing edge noise was well captured using the hybrid RANS-BEM technique.

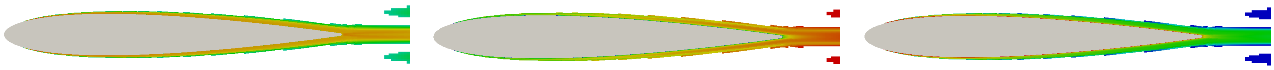

(a) $z/s = 0.9$

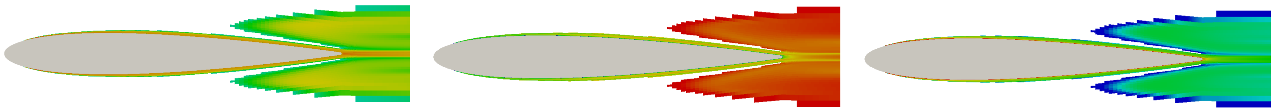

(b) $z/s = 0.95$

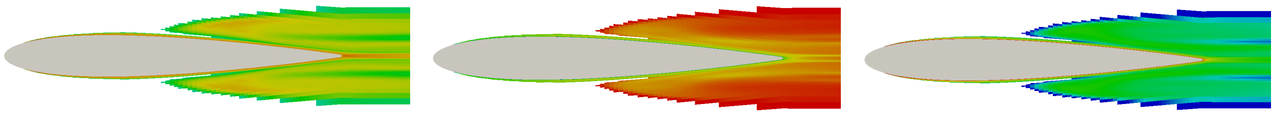

(c) $z/s = 0.975$

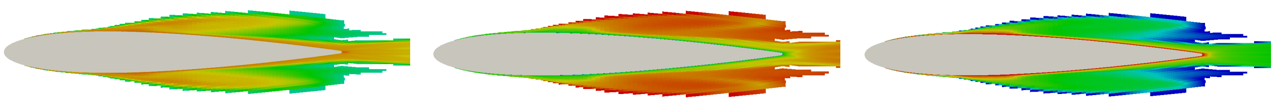

(d) $z/s = 1.0$

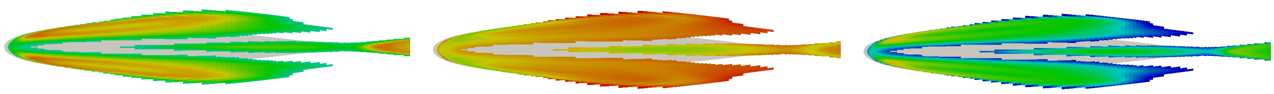

(e) $z/s = 1.013 \times 10^{-2}$

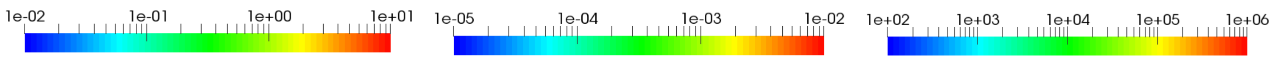

Figure 5: Characteristic velocity (left), length (center) and frequency (right) scales at spanwise planes close to the tip

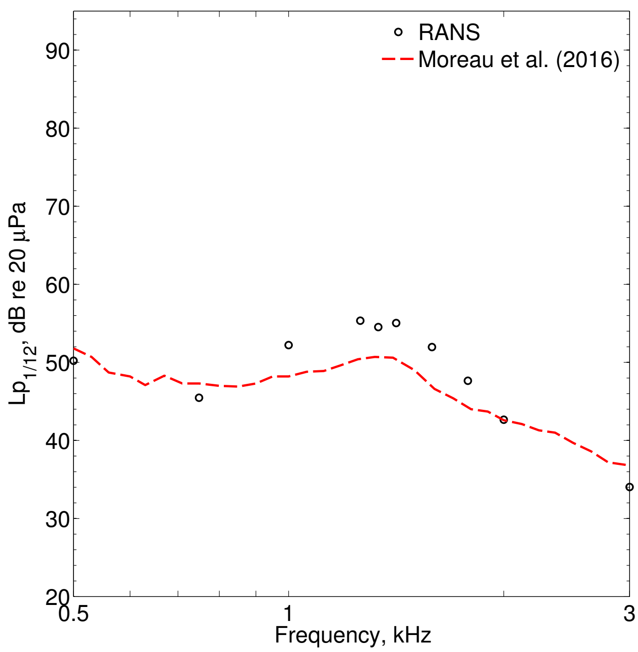

Figure 6: The one-twelfth-octave band level for the entire wall mounted airfoil

REFERENCES

Crighton, DG 1988, 'Goals for computational aeroacoustics', *Computational Acoustics: Algorithms and Applications,* ed. by D, Lee, RL, Sternberg and MH, Schultz, Elsevier.

Croaker, P, Kessissoglou, N and Marburg, S 2015, 'Strongly singular and hypersingular integrals for aeroacoustic incident fields', *International Journal for Numerical Methods in Fluids,* vol. 77, pp. 274–318.

Doolan, C, Albarracin, CA and Hansen, C 2010, 'Statistical estimation of trailing edge noise', *Proceedings of the 20th International Congress on Acoustics,* Sydney, Australia.

Ewert, R 2008, 'Broadband slat noise prediction based on CAA and stochastic sound sources from a fast random particle-mesh (RPM) method', *Computers and Fluids,* vol. 37, pp. 369–387.

Ffowcs Williams, JE and Hall, LH 1970, 'Aerodynamic sound generation by turbulent flow in the vicinity of a scattering half plane', *Journal of Fluid Mechanics,* vol. 40, pp. 657–670.

Fleury, V, Bailly, C, Jondeau, E, Michard, M and Juvé, D 2008, 'Space-time correlations in two subsonic jets using dual particle image velocimetry measurements', *AIAA Journal,* vol. 46, pp. 2498–2509.

He, GW, Yao, HD and Zhao, X 2008, 'Prediction of space-time correlations by large eddy simulations', *Proceedings of the 46th AIAA Aerospace Sciences Meeting and Exhibit,* Reno, Nevada.

Khalighi, Y, Mani, A, Ham, F and Moin, P 2010, 'Prediction of sound generated by complex flows at low Mach numbers', *AIAA Journal,* vol. 48, 2, pp. 306–316.

Marburg, S and Nolte, B, eds. 2008, *Computational Acoustics of Noise Propagation in Fluids,* Springer, Berlin, Germany.

Moreau, DJ, Doolan, CJ, Alexander, WN, Meyers, TW and Devenport, WJ 2016, 'Wall-mounted finite airfoil-noise production and prediction', *AIAA Journal,* vol. 54, 5, pp. 1637–1651.

Ostertag, JSD, Guigati, S, Guidati, G, Wagner, S, Wilde, A and Kalitzin, N 2000, 'Prediction and measurement of airframe noise on a generic body', *Proceedings of the 6th AIAA/CEAS Aeroacoustics Conference,* Lahaina, Hawaii, USA.

Wang, M and Moin, P 2000, 'Computation of trailing-edge flow and noise using large-eddy simulation', *AIAA Journal,* vol. 38, pp. 2201–2209.

Wang, M, Moreau, S, Iaccarino, G and Roger, M 2009, 'LES prediction of wall-pressure fluctuations and noise of a low-speed airfoil', *International Journal of Aeroacoustics,* vol. 8, pp. 177–198.

Zhao, X and He, GW 2009, 'Space-time correlations of fluctuating velocities in turbulent shear flows', *Physical Review E,* vol. 79, p. 046316.